Front. Earth Sci. 2022, 16(3): 657–670
https://doi.org/10.1007/s11707-021-0963-0

RESEARCH ARTICLE

Determination of representative elementary volume of digital coal based on fractal theory with X-ray CT data and its application in fractal permeability predication model

Huihuang FANG (✉)[1,2], Shuxun SANG[3,4,5], Shiqi LIU[3,4,5], Huihu LIU[1,2], Hongjie XU[1,2], Yanhui HUANG[6,1]

1 School of Earth and Environment, Anhui University of Science and Technology, Huainan 232001, China
2 Institute of Energy, Hefei Comprehensive National Science Center, Hefei 230000, China
3 Low Carbon Energy Institute, China University of Mining and Technology, Xuzhou 221008, China
4 School of Resources and Geosciences, China University of Mining and Technology, Xuzhou 221116, China
5 Jiangsu Key Laboratory of Coal-based Greenhouse Gas Control and Utilization,
China University of Mining and Technology, Xuzhou 221008, China
6 State Key Laboratory of Petroleum Resources and Prospecting, China University of Petroleum, Beijing 102249, China

Abstract Representative elementary volume (REV) is the key to study the heterogeneity of digital coal and characterize its macroscopic and microscopic properties. The permeability evolution law of digital coal based on REV analysis can provide theoretical support for the application of permeability prediction model in multi-scale reservoirs. This study takes typical coal samples from Bofang and Sihe coal mines in Qinshui Basin as research object. First, the nondestructive information of two samples is scanned and visualized. Secondly, the calculation methods of two-dimensional (2D) and three-dimensional (3D) fractal dimensions of pores and fractures are illustrated. Then, the determination methods of REV based on porosity and fractal dimension are compared. Finally, the distribution pattern of fractal dimension and porosity curves is studied, the relationship between 2D and 3D fractal dimension is characterized, and the application of fractal permeability model in permeability analysis of multi-scale reservoir is further discussed. The REV size varies greatly in different vertex directions of the same sample and between samples, so REV analysis can only be performed in specific directions. When the REV based on fractal dimension is determined, the porosity curve continues to maintain a downward trend and then tends to be stable. The 2D fractal dimension has a positive linear correlation with the 3D fractal dimension, and the porosity can be expressed as a linear function of the fractal dimension. The permeability through REV analysis domain is mainly affected by fractal dimension, dip angle, azimuth angle and maximum fracture length, which is of great significance for exploring permeability evolution law of coal reservoir at different scales. This study is of great significance for enriching the determination methods of REV in digital coal and exploring the permeability evolution law of multi-scale reservoirs.

Keywords representative elementary volume, fractal dimension, permeability, digital coal, X-ray CT, Qinshui Basin

1 Introduction

The representative elementary volume (REV) is the minimum analytical domain that can effectively characterize the macroscopic physical properties of digital coal (Wu et al., 2019a; Fang et al., 2020), which can availably reduce the computer memory and improve the computation speed (Bertrand et al., 2019; Wei et al., 2020). The attribute value obtained at a scale smaller than REV significantly fluctuates, while it tends to be stable when the scale is larger than REV (Fig. 1; Wu et al., 2019a; Fang et al., 2020). The instability of attribute value in region I gradually decreases with the increase of sample size (Fig. 1-I), and which gradually approaches a certain value in region II, so the left boundary of region II can be regarded as the REV of the sample (Fig. 1-II). Some

Received October 25, 2021; accepted December 16, 2021

E-mail: huihuangfang@aust.edu.cn

attribute values will irregularly change again with the further increase of sample size (Fig. 1-III; Bear, 1972; Wu et al., 2019a). Compared with porosity, fractal dimension is one of the key parameters to describe the complexity of pore and fracture systems (Fang et al., 2020). Although it is often used to characterize the structural characteristics of pore and fracture, it is rarely applied in REV analysis of digital coal.

The fractal theory is a mathematical branch proposed by Mandelbrot in 1983, which is mainly used to describe the irregularity in nature (Zhang et al., 2021a; Zhao et al., 2022), and is also widely used to quantitatively characterize the complexity, roughness, orientation and opening degree of pores and fractures in digital coal (Wu et al., 2019b; Li et al., 2020). The box-counting dimension method is a fractal calculation method based on high resolution image (Wu et al., 2019a), which is the most intuitive parameter in the application of fractal theory (Ai et al., 2014; Li et al., 2021). Compared with the N_2 adsorption experiment, the mercury intrusion experiment and the nuclear magnetic resonance experiment (Wang and Mao, 2021; Zhao et al., 2021), the fractal dimension obtained by box-counting dimension method is more convenient and comprehensive. Therefore, the box-counting dimension method deserves further exploration.

Based on high resolution image data, X-ray CT nondestructive scanning technology can characterize the composition of digital coal (Wang et al., 2019a; Fan et al., 2020; Miao et al., 2021; Wang et al., 2021a), and the analysis method of fractal dimension based on box-counting dimension method will be developed, so as to further enrich the in-depth study of REV based on fractal dimension. Some scholars have conducted preliminary studies on porosity and permeability models of porous media based on fractal theory (Miao et al., 2015a; Yang et al., 2019), and the fractal dimension, maximum fracture length and pore size have great influence on the application of such models (Miao et al., 2015b, 2018). Porosity analysis methods based on fractal dimension were rarely studied, and the relationship between 2D and 3D fractal dimension as well as the relationship between fractal dimension and porosity were not thoroughly discussed. It is thus of great significance to further analyze the application of permeability model in multi-scale digital coal.

In this study, typical coal samples collected from Bofang (BF) and Sihe (SH) coal mines in Qinshui Basin are considered as research objects. First, the nondestructive information of samples analyzed is scanned and visualized. Secondly, the calculation methods of 2D and 3D fractal dimension in digital coal are analyzed. Then, the REV determination method based on porosity and fractal dimension is analyzed. Finally, the distribution pattern of fractal dimension and porosity curves after REV determined is studied, the relationship between 2D and 3D fractal dimension, and porosity and fractal dimension are analyzed, and the application of fractal permeability model in permeability analysis of multi-scale reservoirs is further discussed. The main innovations of this study are as follows: (i) REV determination method based on fractal dimension is deeply analyzed; (ii) relationship between porosity-based REV and fractal dimension-based REV is compared and analyzed; (iii) curve distribution pattern of fractal dimension and porosity after REV determined is summarized and analyzed; (iv) relationship between 2D and 3D fractal dimension is compared and analyzed, and the relationship between fractal dimension and porosity is deeply discussed; (v) based on the improved mathematical model, the application of fractal permeability model is studied.

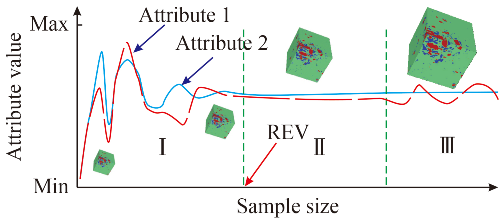

Fig. 1 Change in attribute value as a function of sample size to define REV.

2 Materials and methods

2.1 Geological background

The Qinshui Basin is a mountainous discontinuous basin formed by differential uplift of fault blocks after the coal-forming stage of late Paleozoic in north China, which belongs to the central belt of North China Platform in palaeotectonics, and mainly presents the palaeogeographic background of sea-land interaction in late Paleozoic. At the end of the late Paleozoic, with the closure of the ancient Mongolian ocean, sea water retreated southward, and the interior of the North China Plate was transformed into a large inland lacustrine sedimentary environment (Liu et al., 2021; Zhou et al., 2021). This study area is bounded by the Huo Mountain Fault in the east and the Taihang Mountain Uplift in the west, the Zhongtiao Mountain Uplift in the south, and the Wutai Mountain Uplift in the north (Fig. 2; Wang et al., 2019b; Fang et al., 2021), which is elliptic as a whole with a central contraction and a long axis extending along the NNE direction (Fig. 2(b); Fang et al., 2017). The Taiyuan (i.e., C_2-P_1t) and Shanxi (i.e., P_1s) Formations of Upper Paleozoic are the main coal-bearing systems in this area (Wang et al., 2021b; Zhang et al., 2021b). The No. 15 coal seam of Taiyuan formation and No. 3 coal seam of Shanxi Formation have large thickness and stable distribution, which are the main coalbed methane reservoirs in this area (Fig. 2(c); Fang et al., 2017; Huang et al., 2019; Ni et al., 2020).

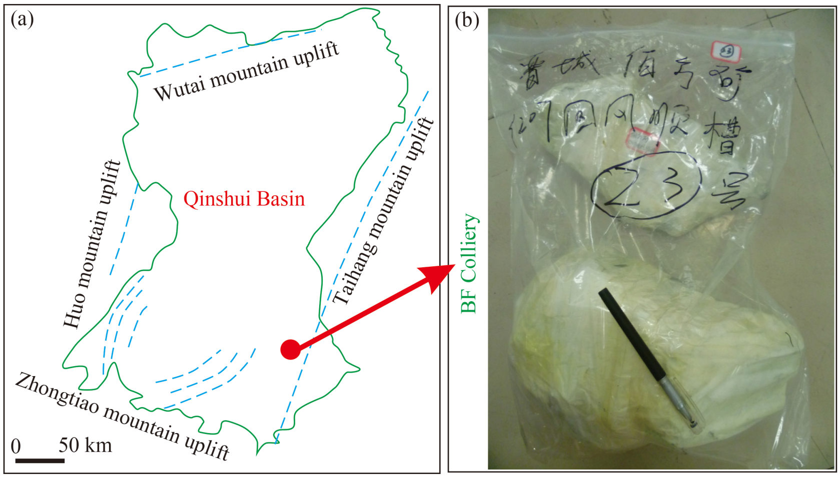

Fig. 2 Geological setting of the Qinshui basin (Modified from Fang et al., 2017). (a) Four uplift belts in the Qinshui basin, and (b) vertical sequences of the sedimentary system of the Shanxi formation.

2.2 Sample collection and basic tests

In this study, the experimental coal samples were selected from the fresh working faces of BF and SH coal mines in Qinshui Basin (Fig. 3; Liu et al., 2017; Fang et al., 2017). The sampling depth is between 200 m and 800 m, the sampling layer is No. 3 coal seam of Shanxi Formation, and the samples were mainly block samples. After stripping from the fresh working faces, coal samples are quickly put into vacuum sealing bags and marked with serial numbers for later use (Fig. 3(c)). Each experiment has different requirements for sample shape and particle size, so, sample preparation should be carried out according to the corresponding national standard (i.e., GB/T 6948-2008 and GB/T 8899-2013; Liu et al., 2017; Fang et al., 2019).

The maximum vitrinite reflectance (i.e., $R_{o,max}$) was measured in accordance with the national standard with GB/T 6948-2008. The maximum oil soaked reflectance of 100 points was counted and the average value was taken as the $R_{o,max}$ of coal samples. The proximate analysis method followed the national standard of GBT 30732-2014. The determination method of macerals analysis was carried out according to the national standard with GBT 8899-2013, and the volume ratio of each maceral was calculated by observing and identifying 500 macerals points by equidistance mobile carrier. Table 1 shows the analysis results of $R_{o,max}$, proximate analysis and macerals analysis of BF and SH samples. Two samples are mainly bright coal, followed by dark coal, and vitrinite is the main organic component. The $R_{o,max}$ of two samples is between 2.83% and 3.33%, and the BF and SH samples are all anthracite (Table 1).

2.3 Sample scanning and visualization analysis

2.3.1 Sample scanning

In this study, coal pillars with a diameter of 2 mm and a length of about 6 mm were used in the X-ray CT

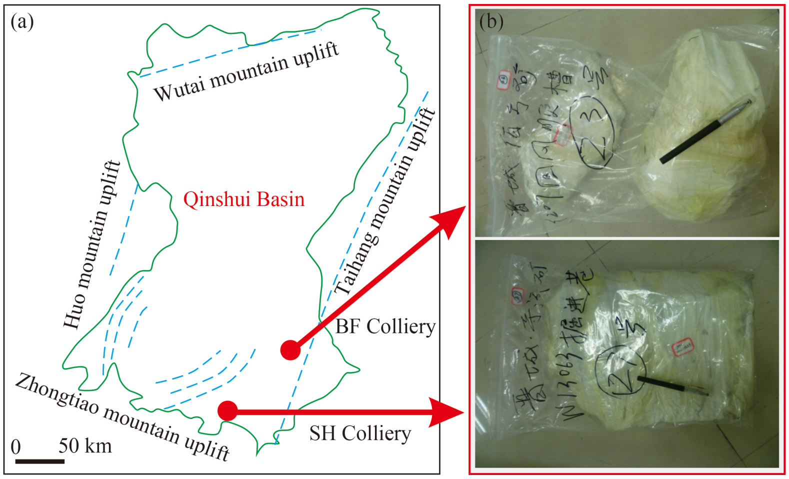

Fig. 3 Sampling point distribution. (a) Location of the Qinshui basin in China and the distribution of sampling point, and (b) Anti-oxidation treatment of coal sample.

Table 1 Key properties of coal sample used in this study.

Sampling location	$R_{o,max}$/%	Proximate analysis /wt.%				Macerals analysis /vol.%		
		M_{ad}	A_{ad}	V_{daf}	FC_{ad}	V_{it}	I_{ne}	M_{in}
BF	2.83	2.05	9.40	9.86	81.67	2.42	91.82	3.85
SH	3.33	1.48	13.12	6.32	81.39	79.84	18.36	1.80

Notes: wt. %, weight percent; vol.%, volume percentage, $R_{o,max/\%,}$ average maximum vitrinite reflectance; M_{ad}, moisture; A_{ad}, ash yield; V_{daf}, volatile matter; FC_{ad}, fixed carbon content; "*ad*", air-drying base; *"daf"*, dry ash-free basis; V_{it}, vitrinite content; I_{ne}, inertinite content; M_{in}, mineral content.

scanning experiment, which was drilled by a mechanical drill prototype (Fig. 4(a)). The experimental equipment is Xradia 520 Versa CT scanner produced by Carl Zeiss, Germany, which is a high-resolution micron focus X-ray digital core analysis system, and is mainly composed of the X-ray source, the precision sample table, the high-resolution detector, the data processing system and the controller system (Fig. 4(b)). The scanning area of X-ray CT was a coal pillar with a diameter of 2 mm and a height of 1 mm. The test voltage was 180 kV, the test current was 50 μA, and the exposure time was 1000 ms. The local scanning mode was adopted with a pixel resolution of 1 μm and a scanning time of 52 min. Based on the above experimental equipment and parameter settings, a series of high-resolution, non-destructive 2D CT slices of coal samples can be obtained (Fig. 4(c)). Among them, the gray, black and white areas in typical slices can characterize the distribution of organic matter, pores and minerals in coal (Fig. 4(c)), and the 3D gray images of coal sample can be obtained by sequential superposition and combination of 2D CT slices.

2.3.2 Visualization analysis

To eliminate the influence of background edge in CT slices, scanned samples were cut into cubes with sides of 600 voxels according to their effective scanning area, which is the analysis domain of this study (Fig. 5(a)). The Median filtering process can well protect the integrity of pores and smooth the transition region between pores and matrix. Therefore, it is often used for noise reduction of original 2D CT slices so as to improve the reconstruction effect and data accuracy in subsequent image processing (Fig. 5(b); Zhou et al., 2016; Ni et al., 2017). In this study, the Digital Terrain Model is used to determine the threshold value of each component of digital coal (Taud et al., 2005; Wu et al., 2019b), and the pore/fracture (i.e., the black area in Fig. 5(c)) and other component (i.e., the white area in Fig. 5(c)) can be segmented, which is called the Binarization process (Zhang et al., 2022).

2.4 Calculation of fractal dimension

2.4.1 Box-counting dimension method

The box-counting dimension method is one of the most commonly used to calculate the fractal dimension of pore and fracture network in digital image (Ai et al., 2014; Wu et al., 2019a, 2019b), which can be expressed by Eq. (1):

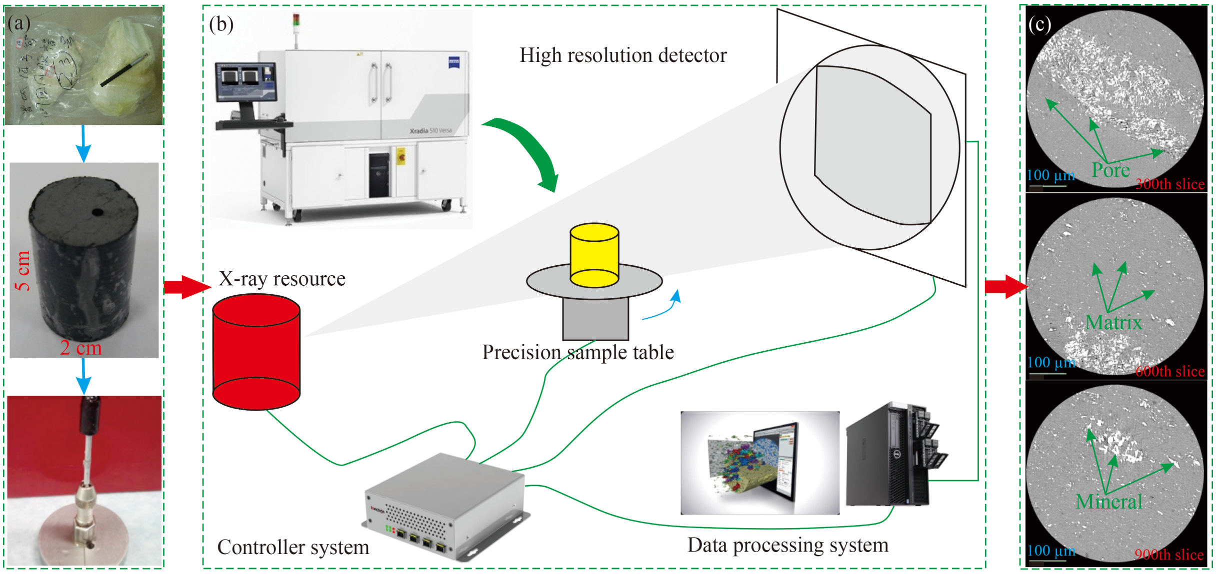

Fig. 4 X-ray CT scanning system using the BF sample as an example. (a) Preparation of sample; (b) imaging system components; (c) typical 2D CT slices of BF sample.

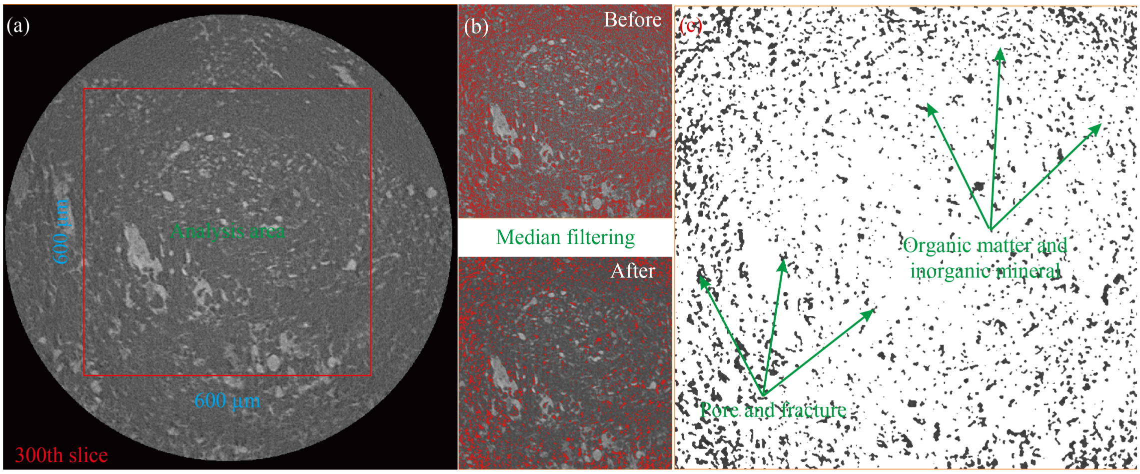

Fig. 5 Image processing flow diagram using the BF sample as an example. (a) Original section; (b) median filtering processing; (c) binarization processing.

$$D_{f,2D/3D} = \lim_{r \to 0} \frac{\log[N(r)]}{-\log(r)}, \quad (1)$$

where D_f is the fractal dimension, $N(r)$ is the number of boxes, that is the sub-analysis domain covering the 3D original cube, and r is the side length of the sub-analysis domain, which can be calculated by dichotomy (He et al., 2021), and the calculation formula is as follows:

$$\delta_k = \frac{1}{r^{k-1}} \left| 0 < k \leqslant \frac{\log \min(x,y,z)}{\log r} \right| + 1 (k = 0,1,2,3\cdots), \quad (2)$$

where x, y, and z represent the side lengths of sub-cubes divided, respectively.

Figure 6 shows the process diagram of calculating fractal dimension based on box-counting dimension method, which mainly includes five core steps: ① determine the side length, r, of the sub-analysis domain according to Eq. (2); ② cover and segment the binarization images of digital coal with boxes of different scales; ③ cumulatively calculate the number of cubes, $N(r)$, covering the pore and fracture space; ④ obtain the set of $(r, N(r))$ by changing the side length of the sub-cubes; ⑤ perform linear fitting between $\log[N(r)]$ and $-\log(r)$, and the slope of the fitting curve is the fractal dimension (Fig. 6).

2.4.2 Calculation of 2D and 3D fractal dimension

For BF and SH samples, the 3D analysis area is 600 μm × 600 μm × 600 μm voxels after eliminating the influence of the background edge in original 2D CT slices (Fig. 5(a) and Fig. 7). In the analysis domain, samples can be cropped from different vertex directions (i.e., from A to H) into sub-analysis domains of different size, which is the regions of interest (i.e., ROI; Fig. 7). Taking vertex B as an example, a sub-analysis domain with side length of 10 voxels (i.e., ROI-1) was first cropped, and then the side length was increased every 10 voxels to generate a larger sub-analysis domain (i.e., ROI-N) until the side length reached the original sample size, which is the 600 voxels in this study (i.e., ROI-60; Fig. 7(b)). In this study, except for 8 cubes with sides of 600 voxels, BF and SH samples can generate 473 sub-analysis domains with different voxels along the 8 vertex directions, respectively. Based on the box-counting dimension method, the 3D fractal dimension of pore and fracture in reconstructed digital coal can be calculated in different

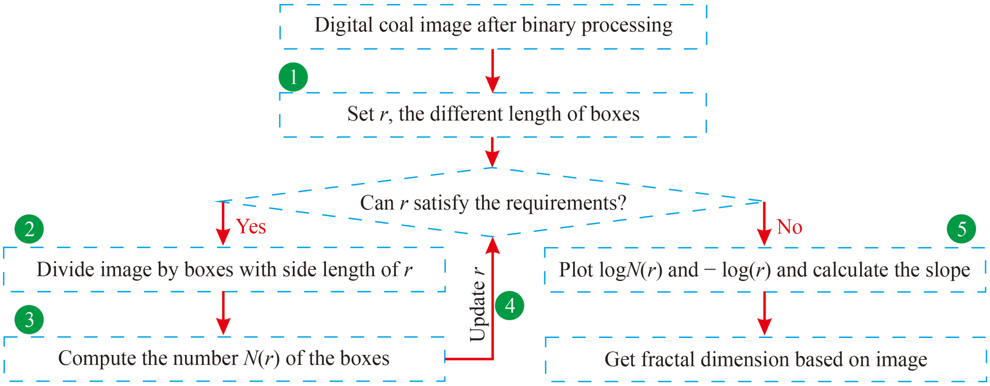

Fig. 6 Schematic diagram of fractal dimension calculation based on the digital coal images.

sub-analysis domains, and for the corresponding 2D slices, the mean value of the fractal dimension of all slices can characterize the 2D fractal dimension.

3 Results and discussion

3.1 REV analysis results based on porosity and fractal dimension

Figures 8 and 9 shows the REV analysis results based on porosity and fractal dimension of BF and SH samples, where the *x*-axis represents the side length of the sub-analysis domain, the *y*-axis on the left symbolizes the 2D/3D fractal dimension, and the *y*-axis on the right characterizes the porosity. It can be seen from Figs. 8 and 9 that the fractal dimension fluctuates significantly in smaller sub-analysis domains. When the size of the sub-analysis domain exceeds a certain critical value, the fractal dimension remains unchanged, and the critical value of side length is the sample REV determined by the fractal dimension. When the side length of the sub-analysis domain is short, that is, the sample size is small, the variation range of porosity and 2D/3D fractal dimension is large, which is consistent with the region in Fig. 1-I (i.e., the red area in Figs. 8 and 9). With the increase of sample size, each attribute curve tends to be stable, which characterizes the area in Fig. 1-II (i.e., the gray area in Figs. 8 and 9). From the perspective of 2D/3D fractal dimension, REV always exists in the sample, but not always exist in certain vertex directions based on porosity data, such as the Figs. 9-D/E/H, which indicates that REV can only be selected in certain specific vertex directions for some coal samples.

Due to the heterogeneity of coal reservoir, the REV sizes vary greatly in different vertex directions of the same sample and between samples (Figs. 8 and 9; Table 2). Therefore, the REV corresponding to the 2D/3D fractal dimension and porosity curve when it stabilizes at the latest is specified as the REV for the whole sample. For BF and SH samples, the REV corresponding to 2D fractal dimension is 370 μm and 365 μm, the REV corresponding to 3D fractal dimension is 325 μm and 382 μm, and the REV corresponding to porosity is 462 μm and 395 μm in analysis domain, respectively (Figs. 8 and 9; Table 2). Therefore, in this study, the REV of BF and SH samples are 462 μm and 395 μm, respectively, and the corresponding analysis directions were vertex E and vertex A, respectively (Table 2).

Based on the 3D reconstruction method of digital coal mentioned in Section 2.3 and the REV size analyzed in Section 3.1, the 3D visual reconstruction of pore and fracture in BF and SH samples was realized (Fig. 10). The maximum REV in the BF sample appears on vertex E, and that of the SH sample appears on vertex A (Fig. 10).

3.2 Distribution pattern of curve between porosity and fractal dimension after REV determined

When REV is determined on the basis of porosity or fractal dimension, the curve distribution of fractal dimension and porosity exists in the following four cases (Fig. 11), where the REV based on fractal dimension takes the largest REV determined by 2D and 3D fractal dimension as the criterion. Case 1: when the fractal dimension curve tends to be stable, REV based on fractal dimension is determined. At this time, the porosity curve continues to maintain a downward trend and then tends to be stable (Fig. 11(a)). Case 2: when the fractal dimension curve tends to be stable, REV based on fractal dimension is determined, and the porosity curve also tends to be stable. In addition, REV based on porosity and REV based on fractal dimension have the same size, and all curves remain stable after REV is determined (Fig. 11(b)). Case 3: when the porosity curve tends to be stable, REV

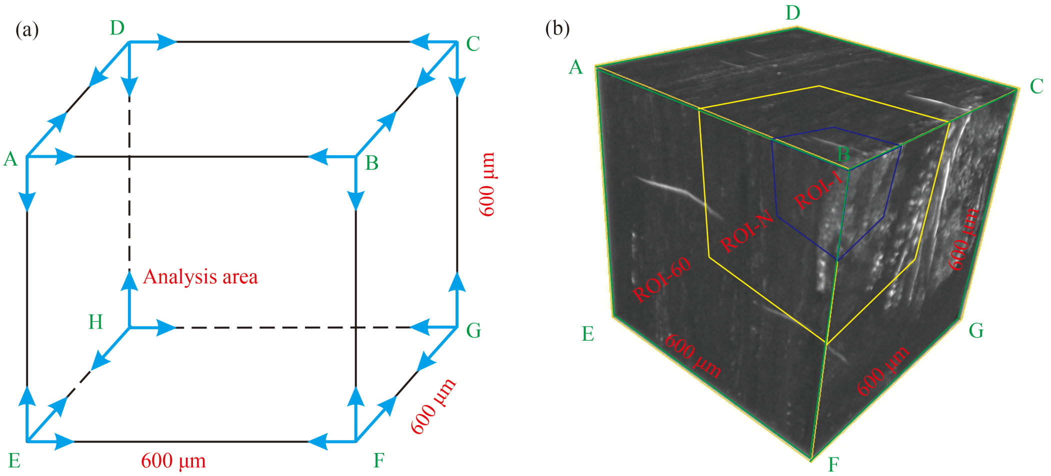

Fig. 7 Schematic diagram of sub-analysis domain selection. (a) Eight vertex directions of A, B, C, D, E, F, G and H in analysis area; and (b) An example of 3 different 3D images that initialized from position B are highlighted with different color.

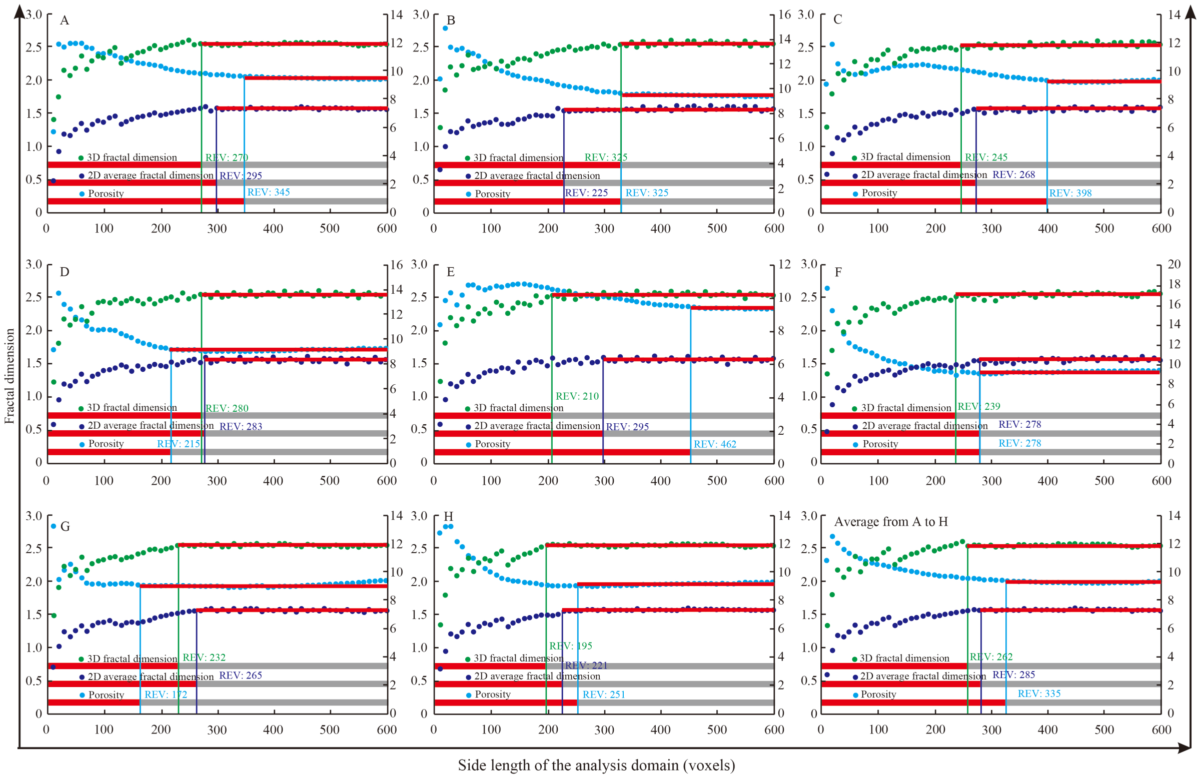

Fig. 8 Results of porosity-based REV and fractal dimension-based REV of BF sample.

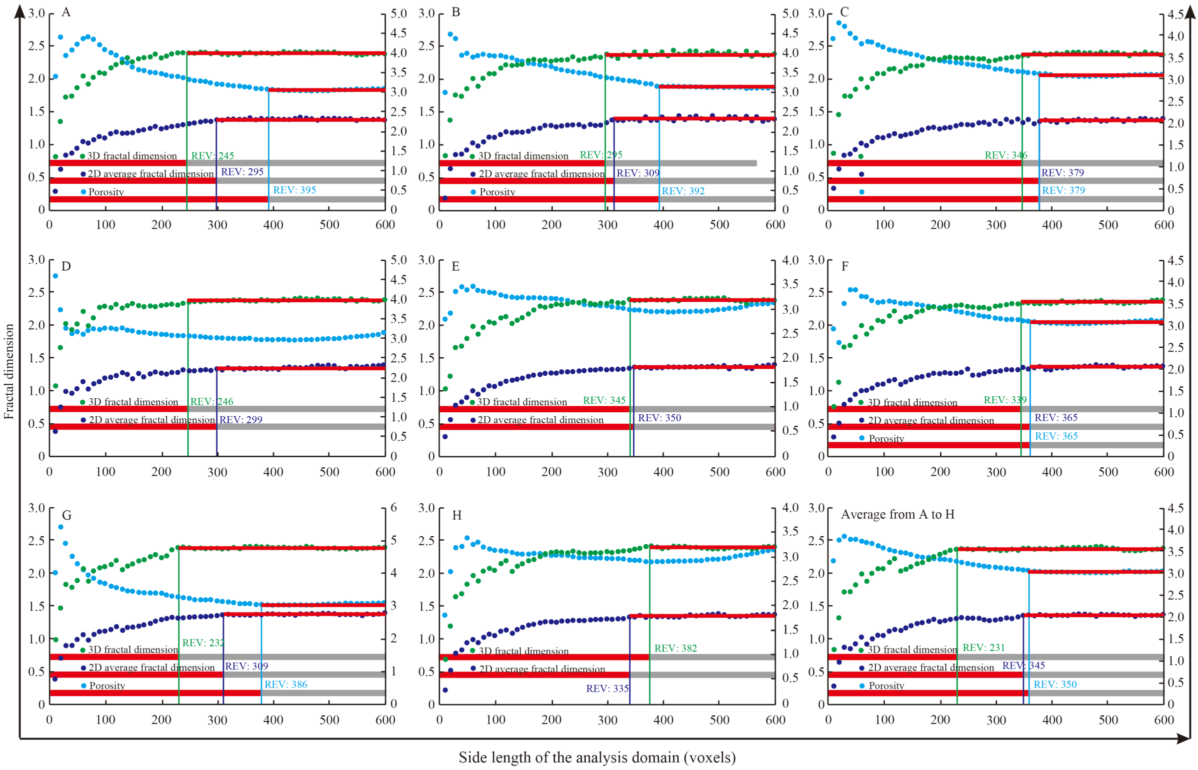

Fig. 9 Results of porosity-based REV and fractal dimension-based REV of SH sample.

Table 2 Porosity-based REV and fractal dimension-based REV with different vertexes of BF and SH samples

Sample	Parameter	A	B	C	D	E	F	G	H	
BF	$D_{f,3D}$	270	325	245	280	210	239	232	195	325
	$D_{f,2D}$	295	325	268	293	295	278	265	221	370
	Porosity	345	225	398	215	462	278	172	251	462
SH	$D_{f,2D}$	245	295	346	249	345	339	232	382	382
	$D_{f,3D}$	295	309	379	299	350	365	309	335	365
	Porosity	395	392	379	---	---	365	386	---	395

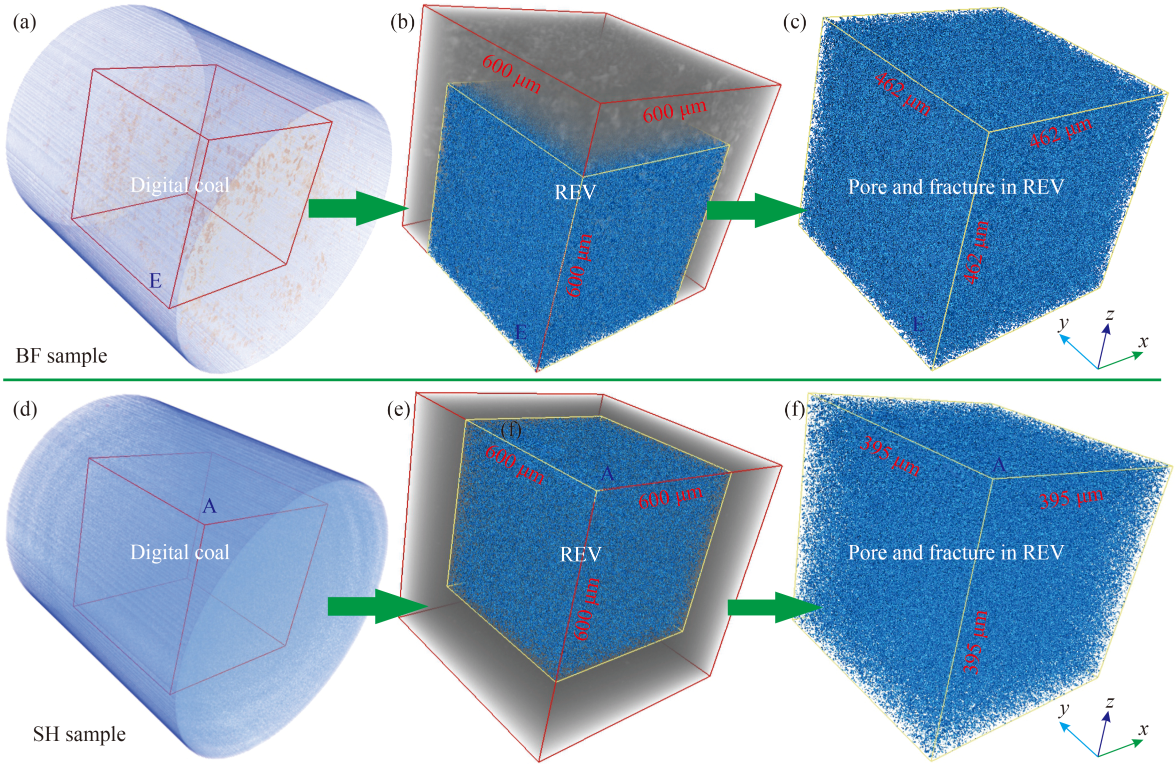

Fig. 10 Pore and fracture structures of digital coal based on the selected REV. (a)–(c) are BF sample; and (d)–(f) are SH sample.

based on porosity is determined. At this time, the curve of fractal dimension keeps rising and then tends to be stable (Fig. 11(c)). Case 4: when the fractal dimension curve tends to be stable, REV based on fractal dimension is determined. At this time, the porosity curve first maintains a stable trend and then tends to increase (Fig. 11(d)). In all cases, when REV is determined for one of the parameters, the curve change of the other parameter is small (Fig. 11).

Table 3 shows the statistical results of curve distribution patterns of fractal dimension and porosity in BF and SH samples after REV determined. The results show that Case 1 is the most typical distribution mode of fractal dimension and porosity curves (Table 3), that is, when the fractal dimension curve tends to be stable, REV based on fractal dimension is determined, and the porosity curve keeps a downward trend and then tends to be stable.

3.3 Relationship between 2D and 3D fractal dimension

As for the relationship between 2D and 3D fractal dimension, previous studies have shown that when the porosity is 1, the 3D fractal dimension is 3, the corresponding 2D fractal dimension is 2, so $D_{f,3D}$ is equal to $D_{f,2D} + 1$ (Wu et al., 2019b). But as far as coal reservoir is concerned, its porosity is much less than 1. In this study, the porosity of BF and SH samples is 9.38% and 3.14%, respectively, so the applicability of the above relationship is not universal. Based on box-counting dimension method, the 2D and 3D fractal dimension in different sub-analysis domains along 8 vertices directions of BF and SH samples are linearly fitted, respectively (Fig. 12).

According to the fitting curve in Fig. 12, the relationship between 2D and 3D fractal dimension can be shown as follows:

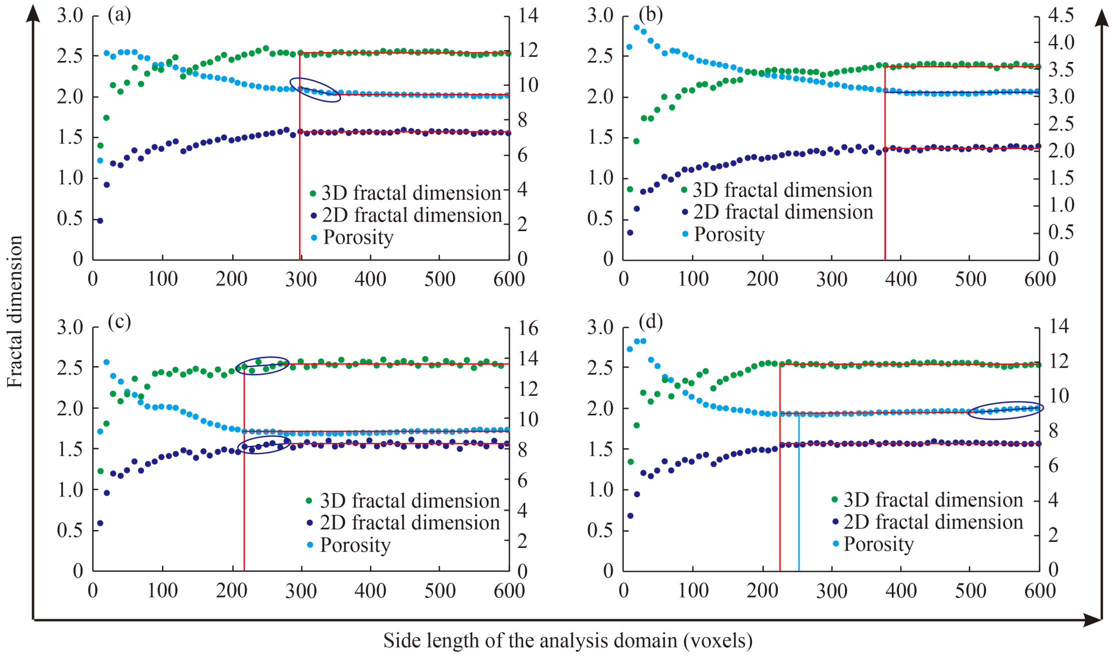

Fig. 11 Distribution pattern of curve between porosity and fractal dimension after REV determined. (a) Vertex direction A of BF sample; (b) vertex direction C of SH sample; (c) vertex direction D of BF sample; (d) vertex direction H of BF sample.

Table 3 Statistical results of curve distribution patterns of fractal dimension and porosity in BF and SH samples

Case	1	2	3	4	No REV
Number	6	3	3	1	3

$$D_{fi,\mathrm{3D}} = M_i D_{fi,\mathrm{2D}} + N_i \ (i = A, B, ..., H), \tag{3}$$

where M_i and N_i are parameters characterizing the relationship between 2D and 3D fractal dimension, and the statistics of which in different sub-analysis domains along 8 vertices directions of BF and SH samples are shown in Table 4.

According to Table 4, there is a positive correlation between 2D and 3D fractal dimension. On the same sample, the data of parameters M_i and N_i in different vertex directions have little difference, and the data difference between different samples is also small. For BF and SH samples, Eq. (3) can be concretized into Eqs. (4)–(5):

$$D_{f,\mathrm{3D}} = 1.202938 D_{f,\mathrm{2D}} + 0.689863, \tag{4}$$

$$D_{f,\mathrm{3D}} = 1.178513 D_{f,\mathrm{2D}} + 0.782425. \tag{5}$$

According to Eqs. (4)–(5), when the porosity is 1, $D_{f,\mathrm{2D}}$ is 2, and the 3D fractal dimension of BF and SH samples are 3.095739 and 3.126685, respectively, and the 3D fractal dimension is approximately 3, which verifies the correctness of Eq. (3).

3.4 Relationship between porosity and fractal dimension

Katz and Thompson (1985) proposed the correlation between porosity and fractal dimension, which was modified by Yu and Li (2001) to make it applicable to a broader field:

$$\varphi = g(r_{\min}/r_{\max})^{d-D_f}, \tag{6}$$

where φ is porosity; g is the parameter; $r_{\max}$ and $r_{\min}$ are the maximum and minimum aperture in the analysis domain, respectively; D_f is the fractal dimension; and d is the Euclidean dimension of the analysis domain, which is 2 and 3 in 2D and 3D dimension, respectively.

Taking logarithmic analysis of both sides of Eq. (6), the correlation between porosity and fractal dimension can be rewritten as follows:

$$\ln\varphi = d\ln[g(r_{\min}/r_{\max})] - D_f \ln[g(r_{\min}/r_{\max})]. \tag{7}$$

Eq. (7) can be further simplified and rewritten as follows:

$$\ln\varphi = mD_f + n, \tag{8}$$

where $m = -\ln[g(r_{\min}/r_{\max})]$, and $n = d\ln[g(r_{\min}/r_{\max})]$.

For BF and SH samples, the 2D/3D fractal dimension and porosity fitting analysis were carried out with typical 2D slices and 3D digital coal as the analysis objects (Figs. (13)–(14)).

With $D_{f,\mathrm{2D}}$ and $D_{f,\mathrm{3D}}$ as horizontal axis, and lnφ as vertical axis, the distribution of data points has a good linear relationship, and the fitted curves all meet Eq. (8) (Figs. (13)–(14)). Theoretically, reservoir porosity can be expressed as a linear function of both 2D and 3D fractal dimension, and the ratio of the minimum pore size to the maximum pore size for samples can be calculated from the slope of the trend line (Figs. (13)–(14)).

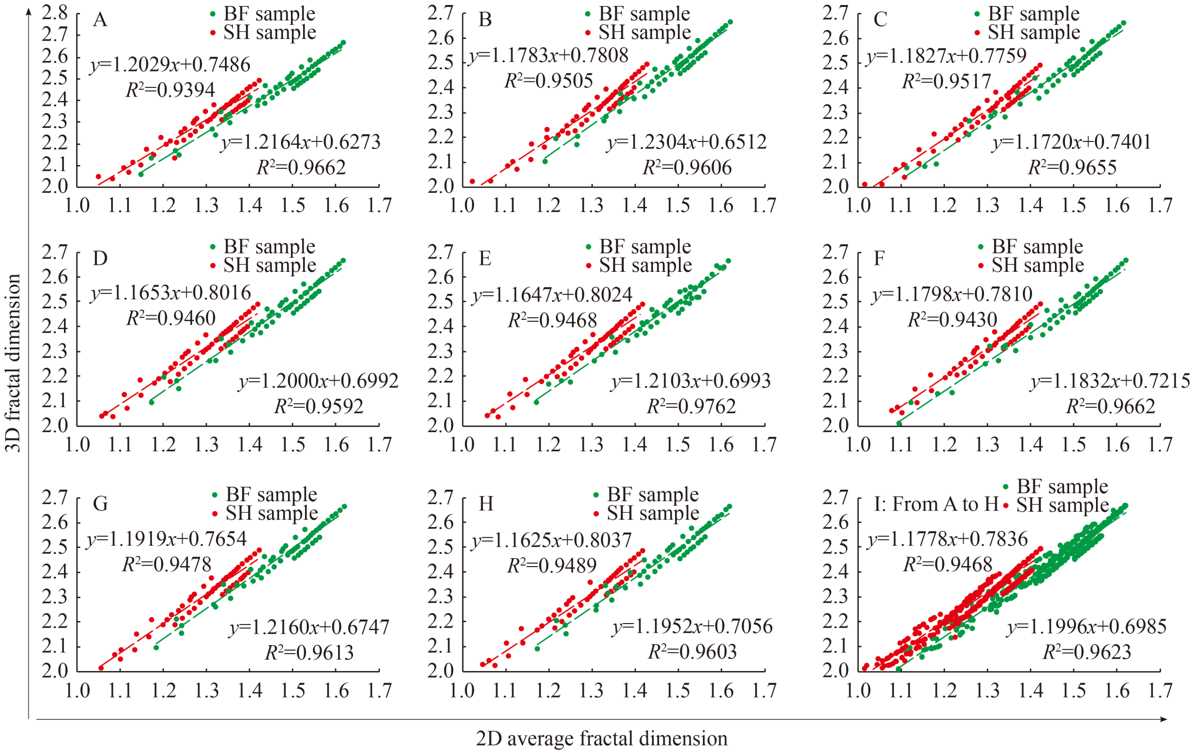

Fig. 12 Relationship between 2D and 3D fractal dimension. A, B, C, D, E, F, G and H are the data of 8 vertex directions, and I is all the data from A to H.

Table 4 Data statistics of parameters M_i and N_i between 2D and 3D fractal dimension of BF and SH samples

Sample	Parameter	A	B	C	D	E	F	G	H	Ave.
BF	M_i	1.2164	1.2304	1.1720	1.2000	1.2103	1.1832	1.2160	1.1952	1.202938
	N_i	0.6273	0.6512	0.7401	0.6992	0.6993	0.7215	0.6747	0.7056	0.689863
SH	M_i	1.2029	1.1783	1.1827	1.1653	1.1647	1.1798	1.1919	1.1625	1.178513
	N_i	0.7486	0.7808	0.7759	0.8016	0.8024	0.7810	0.7654	0.8037	0.782425

3.5 Application in fractal permeability model in multi-scales digital coal

The azimuth angle and inclination angle of fracture are the main factors affecting fluid migration in coal reservoir (Miao et al., 2015b), and the average value is often taken in this study due to the large number of fractures (Nazridoust et al., 2006). To apply the fractal permeability model to multi-scales digital coal, it is assumed that the average inclination angle of fracture between the direction of fracture and fluid flow is α, and the average azimuth angle of the fracture perpendicular to the direction of fluid flow is β (Fig. 15).

The fluid flow in coal reservoir can be characterized by Eq. (9) (Nazridoust et al., 2006):

$$q(l) = \frac{h^3 r}{12\mu}\frac{\Delta P}{r_i}, \tag{9}$$

where q is the flow; h is the fracture aperture; r is the length of fracture trace; μ is the dynamic viscosity; $\triangle P$ is the pressure difference; and r_i is the side length of REV.

It can be seen from Fig. 15 that the fracture tracing length r, and the average inclination angle α, and azimuth angle β, satisfy Eq. (10) (Nazridoust et al., 2006; Miao et al., 2015b):

$$r = 1 - \sin^2\alpha\cos^2\beta. \tag{10}$$

Therefore, Eq. (9) can be further rewritten as Eq. (11):

$$q(r) = \frac{a^3 r(1-\sin^2\alpha\cos^2\beta)}{12\mu}\frac{\Delta P}{r_i}. \tag{11}$$

Based on Eq. (11), integrating REV from the minimum size to the maximum size can obtain the total flow through all fractures, which satisfies Eq. (12) as follows:

$$\begin{aligned} Q &= -\int_{r_{\min}}^{r_{\max}} q(r)\mathrm{d}N(r) \\ &= \frac{\eta^3}{128\mu}\frac{D_f(1-\sin^2\alpha\cos^2\beta)}{4-D_f}\frac{\Delta P}{r_0}r_{\max}^4\left[1-\left(\frac{r_{\min}}{r_{\max}}\right)^{4-D_f}\right], \end{aligned} \tag{12}$$

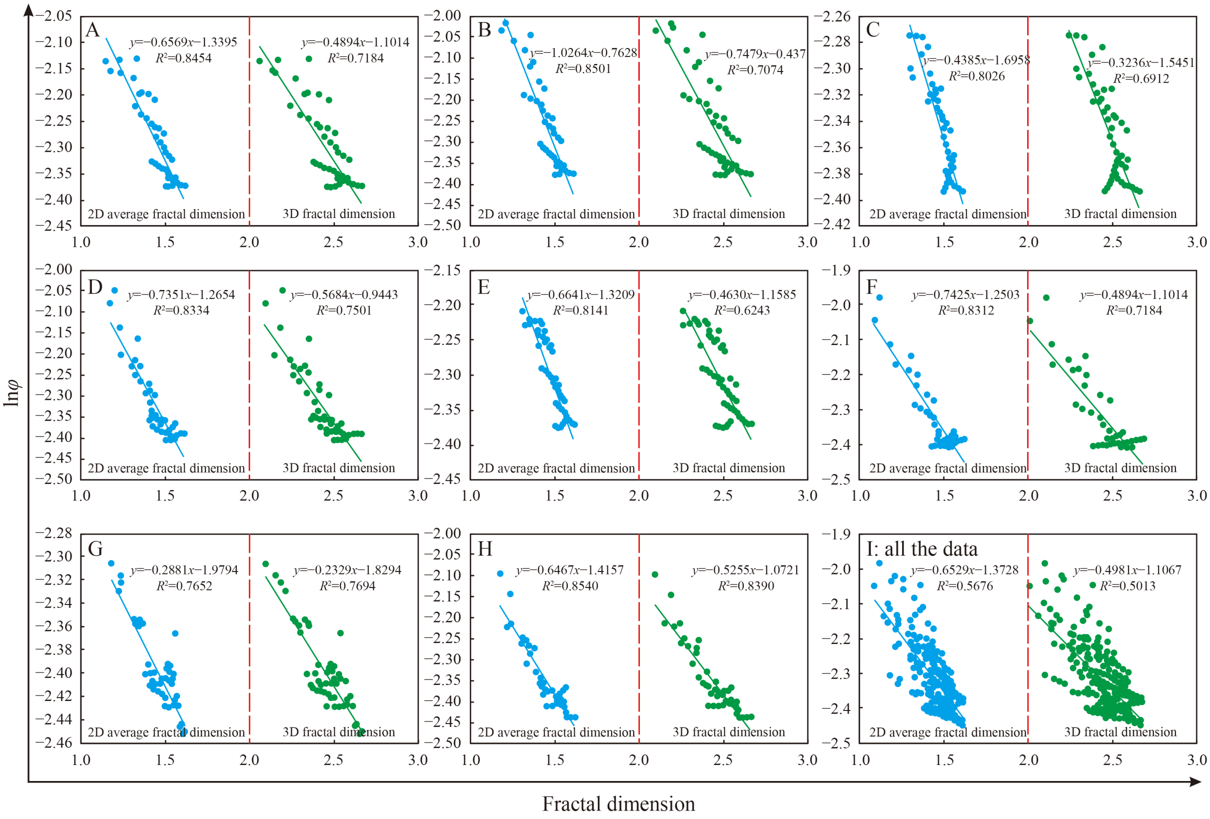

Fig. 13 Relationship between 2D/3D fractal dimension and porosity of BF sample.

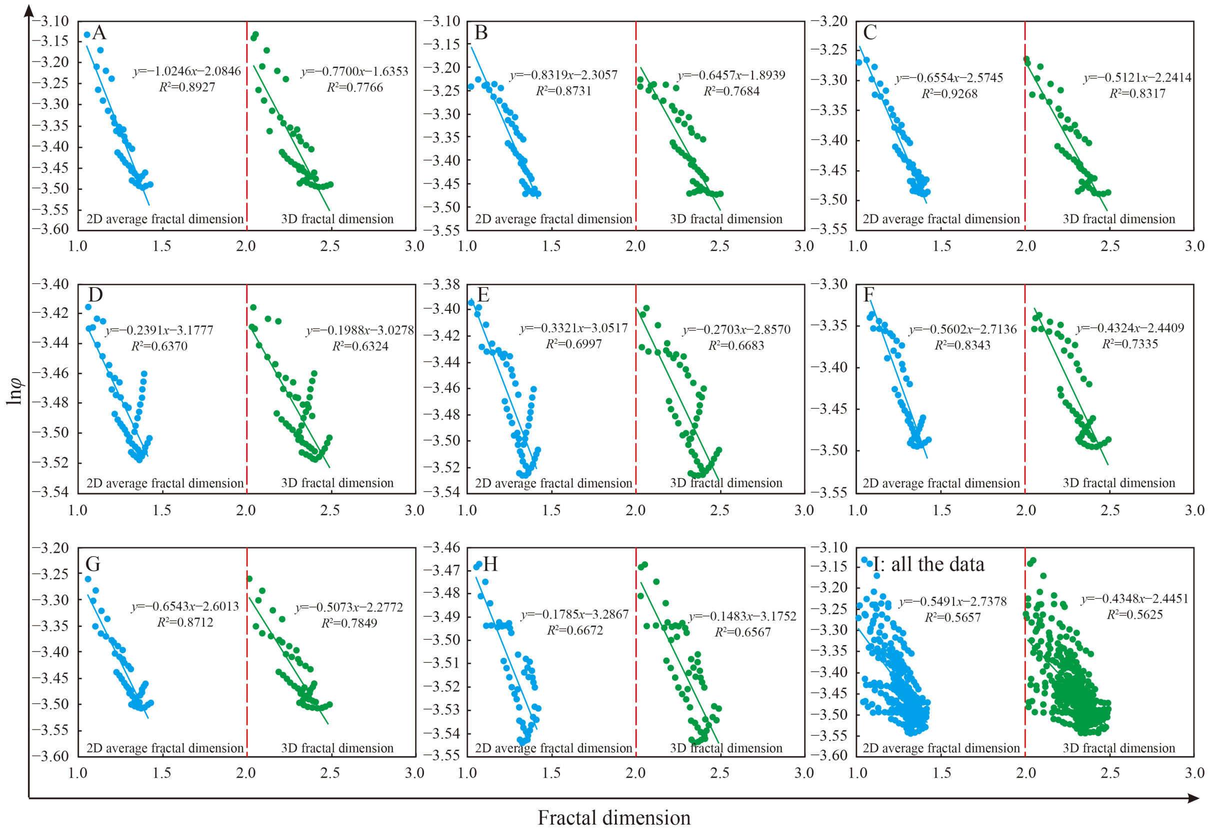

Fig. 14 Relationship between 2D/3D fractal dimension and porosity of SH sample.

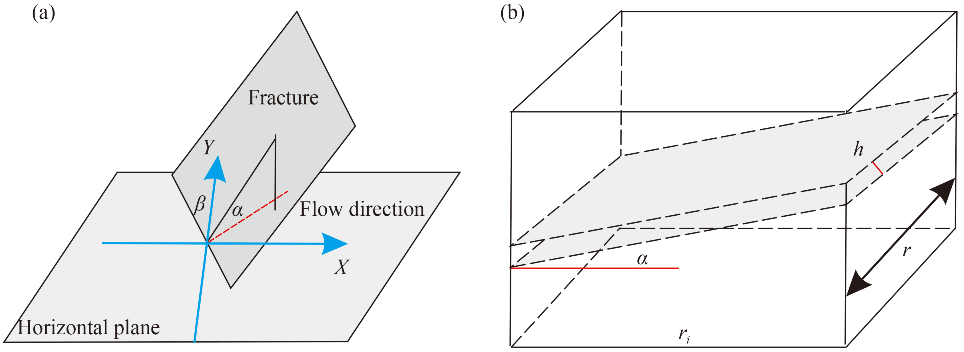

Fig. 15 Schematic diagram of inclination angle (α) and azimuth angle (β) of fracture (Modified from Miao et al., 2015). (a) Diagram of fracture distribution and fluid migration direction; (b) fracture distribution within REV, where r_i is the length of REV, r is the fracture trace length, h is the fracture aperture, α is the fracture plane dip angle with respect to the fluid flow direction at $\beta = 0$.

where D_f is the fractal dimension. In general, the $r_{\min} << r_{\max}$, and $1 < D_f < 3$. Therefore, Eq. (12) can be further simplified to Eq. (13):

$$Q = -\int_{r_{\min}}^{r_{\max}} q(r)\mathrm{d}N(r) = \frac{\eta^3}{128\mu}\frac{D_f(1-\sin^2\alpha\cos^2\beta)}{4-D_f}\frac{\Delta P}{r_0}r_{\max}^4, \tag{13}$$

where η is the proportional coefficient, which is mainly affected by fracture toughness, Poisson’s ratio and young’s modulus (Klimczak et al., 2010; Wu et al., 2019a). According to Eq. (13), the fluid flow rate is mainly affected by fractal dimension, average inclination, average azimuth, and maximum fracture length.

In coal reservoir, the fluid flow also satisfies Darcy’s law:

$$Q = \frac{KA}{\mu}\frac{\Delta P}{r_i}. \tag{14}$$

By comparing Eq. (13) with Eq. (14), it can be obtained that the permeability of fluid through the fracture meets Eq. (15) as follows:

$$K = \frac{Q\mu r_i}{A\Delta P} = \frac{\eta^3}{128A}\frac{D_f(1-\sin^2\alpha\cos^2\beta)}{4-D_f}r_{\max}^4, \tag{15}$$

where K is Darcy permeability; A is the cross sectional area of fluid flow in REV, which is mainly affected by fractal dimension and porosity, and can be characterized as Eq. (16) (Miao et al., 2015b; Wu et al., 2019a), which are as follows:

$$A = \frac{\eta D_f r_{\max}^2}{2-D_f}\frac{1-\varphi}{\varphi}. \tag{16}$$

Therefore, Eq. (15) can be further rewritten as Eq. (17):

$$K = \frac{\eta^2}{12}\frac{\varphi}{1-\varphi}\frac{(2-D_f)(1-\sin^2\alpha\cos^2\beta)}{4-D_f}r_{\max}^2. \tag{17}$$

Assuming α, β, and η are constants, the permeability is mainly affected by φ, D_f, and $r_{\max}$. Therefore, the permeability of multi-scales digital coal can be predicted only by estimating the relationship between φ, D_f, $r_{\max}$ and REV. From the previous analysis in Section 3.1, it can be seen that fractal dimension always exists REV, and $r_{\max}$ is also related to REV, but REV based on porosity does not always exist. When REV was determined based on fractal dimension, not all samples showed a downward trend in porosity. Therefore, this study mainly discusses the most common Case 1 (Table 3), that is, the fractal dimension remains constant with the increase of the computational domain, while the porosity decreases.

According to the fitted trend line in the case in Section 3.4, the relationship between porosity and REV size can be calculated as follows:

$$\varphi = ur + v, \tag{18}$$

where u and v are constants.

The maximum fracture length is also a function of side length, which satisfies the following formula:

$$r_{\max} = \frac{r}{\cos\theta}. \tag{19}$$

Based on Eqs. (18) and (19), Eq. (17) can be further rewritten into Eq. (20) as follows:

$$K = \frac{\eta^2}{12}\frac{ur+v}{1-ur-v}\frac{(2-D_f)(1-\sin^2\alpha\cos^2\beta)}{4-D_f}\frac{r^2}{\cos^2\alpha}. \tag{20}$$

When REV is determined on the basis of fractal dimension, the only variable in Eq. (20) is side length r. Therefore, Eq. (20) can be used to predict the permeability of fluid migration at different scales in coal reservoirs.

4 Summary and conclusions

This study takes two samples as the research object. First, the nondestructive information of samples is scanned and visualized. Secondly, the calculation methods of 2D and 3D fractal dimension in digital coal are illustrated. Then, the determination methods of REV based on porosity and fractal dimension are compared. Finally, the distribution pattern of fractal dimension and porosity curves is studied, the relationship between 2D and 3D fractal dimension is characterized, and the application of fractal permeability model in permeability analysis of multi-scale reservoirs is further discussed. The main conclusions are as follows.

1) REV sizes vary greatly in different vertex directions of same sample and between samples. With the increase of sample capacity, the porosity and 2D/3D fractal dimension curves tend to be stable, and the REV corresponding to the 2D/3D fractal dimension and porosity curve when it stabilizes at the latest is specified as the REV for the whole sample. Based on 2D/3D fractal dimension, REV always exists in the sample, but not always in certain vertex directions based on porosity data, which indicates that REV can only be selected in certain specific vertex directions for some coal samples.

2) When REV is determined based on fractal dimension, the curve distribution of porosity exists in the following four cases. Case 1: the porosity curve continues to maintain a downward trend and then tends to be stable. Case 2: the porosity curve also tends to be stable. Case 3: the curve of fractal dimension keeps rising and then tends to be stable. Case 4: the porosity curve first maintains a stable trend and then tends to increase.

3) The 2D fractal dimension has a positive linear correlation with the 3D fractal dimension, and the difference of slope and intercept of all fitting curves was small in different vertex directions of the same sample and between samples. Porosity can be expressed as a linear function of both 2D and 3D fractal dimension, and the ratio of the minimum pore size to the maximum pore size for each sample can be calculated from the slope of the trend line.

4) The azimuth angle and inclination angle of fracture are the main factors affecting fluid migration. The flow through the cross section is mainly affected by D_f, α, β, and $r_{\max}$, and permeability is mainly influenced by φ, D_f and $r_{\max}$. By estimating the relationship between φ, D_f and $r_{\max}$ and REV, the permeability in multi-scales digital coal can be predicted. When REV is determined, the permeability of fluid migration is mainly determined by the edge length of analytical domain of digital coal.

Acknowledgment We would like to express our gratitude to the anonymous reviewers for offering their constructive suggestions and comments which improved this manuscript in many aspects. This work was financially supported by the National Natural Science Foundation of China (Grant No. 42102217), the University Synergy Innovation Program of Anhui Province (No. GXXT-2021-018), the Natural Science Research Project of Anhui University (Nos. KJ2020A0315 and KJ2020A0317), the Natural Science Foundation of Anhui Province (No. 2108085MD134), and the Foundation of State Key Laboratory of Petroleum Resources and Prospecting, China University of Petroleum, Beijing (No. PRP/open-2005).

References

Ai T, Zhang R, Zhou H, Pei J (2014). Box-counting methods to directly estimate the fractal dimension of a rock surface. Appl Surf Sci, 314: 610–621

Bear J (1972). Dynamics of Fluids in Porous Media. New York: Elsevier

Bertrand F, Buzzi O, Collin F (2019). Cleat-scale modelling of the coal permeability evolution due to sorption-induced strain. Int J Coal Geol, 216: 103320

Fan N, Wang J, Deng C, Fan Y, Wang T, Guo X (2020). Quantitative characterization of coal microstructure and visualization seepage of macropores using CT-based 3D reconstruction. J Nat Gas Sci Eng, 81: 103384

Fang H, Sang S, Wang J, Liu S, Ju W (2017). Simulation of paleotectonic stress fields and distribution prediction of tectonic fractures at the Hudi coal mine, Qinshui Basin. Acta Geol Sin-Eng, 91(6): 2007–2023

Fang H, Sang S, Liu S, Liu S (2019). Experimental simulation of replacing and displacing CH_4 by injecting supercritical CO_2 and its geological significance. Int J Greenh Gas Control, 81: 115–125

Fang H, Sang S, Liu S (2020). Three-dimensional spatial structure of the macro-pores and flow simulation in anthracite coal based on X-ray μ-CT scanning data. Petrol Sci, 17(5): 1221–1236

Fang H, Sang S, Du Y, Liu H, Xu H (2021). Visualization characterization of minerals touched by interconnected pores and fractures and its demineralization effect on coal permeability during CO_2-ECBM process based on X-ray CT data. J Nat Gas Sci Eng, 95: 104213

He Q, Li F, Shi A, He B, Chen J, Xie L (2021). Fractal characterization of complex hydraulic fracture networks of oil shale via 3D CT reconstruction. Petrol Geo Recov Effi, 28(5): 116−123 (in Chinese)

Huang S, Liu D, Cai Y, Gan Q (2019). In situ stress distribution and its impact on CBM reservoir properties in the Zhengzhuang area, southern Qinshui Basin, north China. J Nat Gas Sci Eng, 61: 83–96

Katz A J, Thompson A H (1985). Fractal sandstone pores: implications for conductivity and pore formation. Phys Rev Lett, 54(12): 1325–1328

Klimczak C, Schultz R, Parashar R, Reeves D (2010). Cubic law with aperture length correlation: implications for network scale fluid flow. Hydrogeol J, 18(4): 851–862

Li Y, Zhao Y, Jiang Y, Zhang B, Song H, Liu B (2020). Characteristics of pore and fracture of coal with bursting proneness based on DIC and fractal theory. Energies, 13(20): 5404

Li Q, Liu D, Cai Y, Zhao B, Lu Y, Zhou Y (2021). Effects of natural micro-fracture morphology, temperature and pressure on fluid flow in coals through fractal theory combined with lattice Boltzmann method. Fuel, 286(2): 119468

Liu S, Sang S, Wang G, Ma J, Wang T, Wang W, Du Y, Wang T (2017). FIB-SEM and X-ray CT characterization of interconnected pores in high-rank coal formed from regional metamorphism. J Petrol Sci Eng, 148: 21–31

Liu R, Ren Z, Yang P, He H, Smith T, Guo W, Wu L (2021). Mesozoic tectono-thermal event of the Qinshui Basin, central north China craton: insights from illite crystallinity and vitrinite reflectance. Front Earth Sci, 9: 765497

Miao T, Yu B, Duan Y, Fang Q (2015a). A fractal analysis of permeability for fractured rocks. Int J Heat Mass Transf, 81: 75–80

Miao T, Yang S, Long Z, Yu B (2015b). Fractal analysis of permeability of dual-porosity media embedded with random fractures. Int J Heat Mass Transf, 88: 814–821

Miao T, Chen A, Xu Y, Cheng S, Wang K (2018). A Permeability model for water-gas phase flow in fractal fracture networks. Fractals, 26(6): 1850087

Miao Z, Li S, Xie J, Huo R, Ding F, Zhu H, Yang X, Li X (2021). Three-dimensional reconstruction and numerical simulation analysis of acid-corroded sandstone based on CT. Shock Vib, 2021: 5582781

Nazridoust K, Ahmadi G, Smith D (2006). A new friction factor correlation for laminar, single-phase flows through rock fractures. J Hydrol (Amst), 329(1−2): 315–328

Ni X, Miao J, Lv R, Lin X (2017). Quantitative 3D spatial characterization and flow simulation of coal macropores based on μCT technology. Fuel, 200: 199–207

Ni X, Zhao Z, Wang Y, Wang L (2020). Optimisation and application of well types for ground development of coalbed methane from No. 3 coal seam in shizhuang south block in Qinshui Basin, Shanxi Province, China. J Petrol Sci Eng, 193: 107453

Taud H, Martinez-Angeles R, Parrot J, Hernandez-Escobedo L (2005). Porosity estimation method by X-ray computed tomography. J Petrol Sci Eng, 47(3−4): 209–217

Wang G, Qin X, Shen J, Zhang Z, Han D, Jiang C (2019a). Quantitative analysis of microscopic structure and gas seepage characteristics of low-rank coal based on CT three-dimensional reconstruction of CT images and fractal theory. Fuel, 256: 115900

Wang X, Wang X, Pan Z, Yin X, Chai P, Pan S, Yang Q (2019b). Abundance and distribution pattern of rare earth elements and yttrium in vitrain band of high-rank coal from the Qinshui Basin, northern China. Fuel, 248: 93–103

Wang Y, Mao C (2021). Nano/micro pore structure and fractal characteristics of Baliancheng coalfield in Hunchun Basin. J Nanosci Nanotechnol, 21(1): 682–692

Wang G, Qin X, Han D, Liu Z (2021a). Study on seepage and deformation characteristics of coal microstructure by 3D reconstruction of CT images at high temperatures. Int J Min Sci Technol, 31(2): 175–185

Wang H, Yao Y, Huang C, Liu D, Cai Y (2021b). Fault development characteristics and their effects on current gas content and productivity of No.3 coal seam in the Zhengzhuang field, southern Qinshui Basin, north China. Energy Fuels, 35(3): 2268–2281

Wei M, Liu J, Elsworth D, Liu Y, Zeng J, He Z (2021). Impact of equilibration time lag between matrix and fractures on the evolution of coal permeability. Fuel, 290: 120029

Wu H, Yao Y, Zhou Y, Qiu F (2019a). Analyses of representative elementary volume for coal using X-ray μ-CT and FIB-SEM and its application in permeability predication model. Fuel, 254: 115563

Wu H, Zhou Y, Yao Y, Wu K (2019b). Imaged based fractal characterization of microfracture structure in coal. Fuel, 239: 53–62

Yang Y, Yang H, Tao L, Yao J, Wang W, Zhang K, Luquot L (2019). Microscopic determination of remaining oil distribution in sandstones with different permeability scales using computed tomography scanning. J Energy Resour Technol, 141(9): 092903, 092903−092911

Yu B, Li J (2001). Some fractal characters of porous media. Fractals, 9(03): 365–372

Zhang G, Guo J, Xu B, Xu L, Dai Z, Yin S, Soltanian M (2021a). Quantitative analysis and evaluation of coal mine geological structures based on fractal theory. Energies, 14(7): 1925

Zhang K, Sang S, Zhou X, Liu C, Ma M, Niu Q (2021b). Influence of supercritical CO_2-H_2O-caprock interactions on the sealing capability of deep coal seam caprocks related to CO_2 geological storage: a case study of the silty mudstone caprock of coal seam no. 3 in the Qinshui Basin, China. Int J Greenh Gas Control, 106: 103282

Zhang P, Zhang C, Liu B, Wu Y (2022). Leveraging local and global descriptors in parallel to search correspondences for visual localization. Pattern Recognit, 122: 108344

Zhao W, Wang K, Wang L, Cheng Y, Dong H, Li B, Dai L (2021). Influence of matrix size and pore damage path on the size dependence of gas adsorption capacity of coal. Fuel, 283: 119289

Zhao Y, Wang C, Ning L, Zhao H, Bi J (2022). Pore and fracture development in coal under stress conditions based on nuclear magnetic resonance and fractal theory. Fuel, 309: 122112

Zhou G, Zhang Q, Bai R, Ni G (2016). Characterization of coal micro-pore structure and simulation on the seepage rules of low-pressure water based on CT scanning data. Minerals (Basel), 6(3): 78

Zhou X, Sang S, Niu Q, Zhang K, Liu F, Wang W, Chang J (2021). Changes of multiscale surface morphology and pore structure of mudstone associated with supercritical CO_2-water exposure at different times. Energ Fuel, 35(5): 4212–4223